



Impacts of X-ray energy and beam size on CD-SAXS measurement precision

Xu-Yang Qin^{1,2,3} · Bing Guo¹ · Nan Pan^{1,2,3} · Xin-Hao Gao^{1,2,3} · Shu-Min Yang² · Chun-Xia Hong² · Ying Wang² · Xiu-Hong Li^{1,2,3} · Chun-Ming Yang^{1,2,3} · Feng-Gang Bian^{1,2,3}

Received: 19 December 2024 / Revised: 18 March 2025 / Accepted: 9 April 2025 / Published online: 2 February 2026

© The Author(s), under exclusive licence to China Science Publishing & Media Ltd. (Science Press), Shanghai Institute of Applied Physics, the Chinese Academy of Sciences, Chinese Nuclear Society 2026

Abstract

With the development of the semiconductor industry below the 7 nm scale, critical dimension small-angle X-ray scattering (CD-SAXS) has emerged as a powerful tool for quantitatively measuring nanoscale deviations. In this study, the effects of X-ray beam size and photon energy on the accuracy of critical dimension measurements were investigated. Critical dimensions measured using beams with different spot sizes showed different deviations from the expected values. Beam sizes that were either too large or too small did not improve confidence intervals. As the incident energy increased, the X-ray transmission rate increased, while the scattering cross section decreased, resulting in a gradual decrease in the signal-to-noise ratio of the diffraction peaks, which reduced the accuracy of the CD-SAXS measurements. An optimal accuracy was obtained at 12 keV with a smaller beam size. Using an effective trapezoid model, the results yielded an average pitch of 100.4 ± 0.2 nm, width of 49.8 ± 0.2 nm, height of 130.0 ± 0.2 nm, and a sidewall angle below $1.1^\circ \pm 0.1^\circ$. These results provide crucial guidance for the future development of CD-SAXS laboratories and the construction of X-ray machines as well as robust support for research in related fields.

Keywords Critical dimension small-angle X-ray scattering · Nonlinear fitting · Beam size · X-ray energy · Chip

1 Introduction

The chip industry is undergoing significant transformation in the rapidly developing fields of microelectronics and nanotechnology. Semiconductor manufacturers are continuously

striving to enhance chip performance, add functionalities, and integrate additional components onto chips [1–7]. With the ongoing improvements in integrated circuits, planar-integrated circuits can no longer meet the needs of development. Thus, advanced processes such as 3D transistor designs and intricate patterning techniques have been developed. Fin-based field-effect transistors (FinFET) remained the mainstream device option until 2021, when gate-all-around (GAA) designs emerged and dominated at smaller dimensions owing to their better electrostatic control. Meanwhile, techniques such as 3D stacking and 3D very-large-scale integration (3DVLSI) have introduced a significant number of additional steps in production processes of integrated circuits [8, 9]. In these processes, the grating serves as a crucial microstructure, that play a vital role in chip manufacturing. With technological advancements, the critical dimensions of chips have gradually decreased, requiring more accurate and high-resolution measurement techniques. The size of the gratings decreases rapidly, which poses considerable challenges for precise measurements.

The work was supported by the National Natural Science Foundation of China (No. 12175295), the National Key R&D Program of China (2021YFA1601000) and the Shanghai Municipal Science and Technology Major Project.

✉ Chun-Ming Yang
yangcm@sari.ac.cn

✉ Feng-Gang Bian
bianfg@sari.ac.cn

¹ Shanghai Institute of Applied Physics, Chinese Academy of Sciences, Shanghai 201800, China

² Shanghai Synchrotron Radiation Facility, Shanghai Advanced Research Institute, Chinese Academy of Sciences, Shanghai 201204, China

³ University of Chinese Academy of Sciences, Beijing 100049, China

In the methods used for the measurement of grating dimensions, scanning electron microscopy (SEM) and atomic force microscopy (AFM) are capable of detecting local critical dimensions in gratings [10]. The optical critical dimension (OCD) is another technology that is widely applied, especially in the study of devices such as nonplanar FinFETs on silicon insulators [11, 12].

Small-angle X-ray scattering has been extensively employed in a multitude of scientific disciplines, including physics, chemistry, materials science, and life sciences, as a highly effective technique for examining structural characteristics at the nanoscale [13–18]. This enables nondestructive analysis of the dimensions, morphology, and distribution of nanoparticles [19] as well as investigation of the structure of biological macromolecules [20, 21], measurement of the size, shape, and size distribution of nanoparticles, and analysis of the microstructure of thin films for solar cells [22, 23]. Notably, the critical dimension small-angle X-ray scattering (CD-SAXS) technique developed by scientists at NIST stands out as a promising measurement platform that can reveal the three-dimensional configuration of regularly spaced arrays of nanostructured surface elements [24, 25]. CD-SAXS has the potential to serve as an alternative to OCD measurement methods. This advanced X-ray scattering technique can be used to explore critical dimensions, morphology, structure, and organization of materials at the nanoscale. Being nondestructive, CD-SAXS enables the measurement of the angle and intensity distribution of X-ray scattering in materials. Its key advantage lies in revealing detailed microstructural information at the nanoscale. By precisely measuring critical dimensions such as line width and spacing, CD-SAXS can contribute to process control and optimization, offering precision at the nanometer scale while remaining nondestructive.

In the field of advanced 3D microelectronics architecture, the outstanding performance of CD-SAXS in providing high-precision critical dimension measurements has been well established [26]. CD-SAXS has been effectively utilized to investigate the widely popular FinFET structures of gratings and has validated its measurement capabilities for potential future grating structures [27]. Roughness critically impacts transistor performance, and CD-SAXS can measure roughness information and exhibits robust characterization potential under various conditions, including synchrotron radiation sources and laboratory environments [28]. Previous research has indicated that the precision of the critical dimensions of the grating are affected by the energy of the X-rays, which highlights the need for further studies on the influence of X-ray energies on measurement accuracy. This technology has marked significant advancements in addressing grating roughness issues, and important insights have been provided on methods to optimize transistor performance [29, 30]. Notably, CD-SAXS experiments conducted

under synchrotron radiation sources not only provide highly accurate data for grating roughness but also lay the foundation for the design and optimization of future grating structures. Furthermore, the successful application of CD-SAXS in laboratory environments has promoted the development and spread of CD-SAXS technology. In summary, CD-SAXS demonstrates remarkable potential in 3D microelectronic architectures, offering powerful tools and methods for studying grating structures.

Currently, CD-SAXS primarily uses synchrotron radiation as its X-ray source. Although synchrotron radiation can meet the requirements of high brightness and sensitivity, CD-SAXS applications using laboratory X-ray sources still involve some notable limitations. Establishing laboratory X-ray sources is crucial to address the challenges associated with the high cost and constrained experimental conditions of synchrotron sources and to expand the application domains of the technology. The selection of target materials for laboratory X-ray sources is a critical step in determining the X-ray energy spectra to meet specific requirements of grating measurements. Additionally, the influence of beam size on measurement precision has not been systematically investigated in previous studies. In this study, we investigated the effects of varying beam size and X-ray photon energies on CD-SAXS experimental accuracy were examined.

2 Experimental and calculation methods

CD-SAXS measurements were conducted at the small-angle X-ray scattering beamline of the Shanghai Synchrotron Radiation Facility (SSRF). Measurements were conducted with 12 keV photons at the center position of the sample and utilized four different beam sizes. Additionally, a further series of measurements was performed at the same sample position with the same beam size with three different photon energies.

2.1 Critical dimension small-angle X-ray scattering

CD-SAXS measurements were conducted on a trapezoidal sample shown in Fig. 1, which illustrates a grating model with a trapezoidal profile characterized by several geometrical parameters, including pitch L , height h , width W , sidewall angle (SWA) θ , and the roughness of the sidewall.

In this study, we utilized transmission small-angle X-ray scattering through a silicon substrate with a thickness of 0.7 mm. The measurement geometry, as elaborated in Fig. 2, specifies the \mathbf{q} vectors for both the beam and the detector. The configuration aligns the Z -direction with the incoming beam, while the X - and Y -directions are set perpendicular to both the

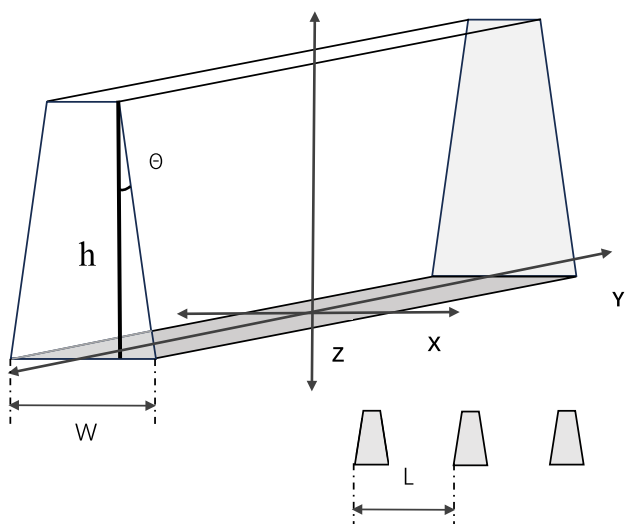


Fig. 1 Schematic representation of the structural parameters of trapezoidal line gratings in Cartesian coordinates, where w is the bottom width, h is the height, L is the period, and θ is the sidewall angle of the line cross sections

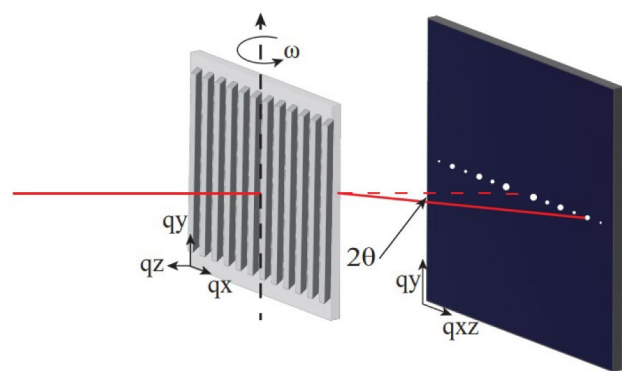


Fig. 2 (Color online) The CD-SAXS geometry illustrates the orientations of the \mathbf{q} vector at both the sample and detector. The sample's center of rotation aligns with the incident beam, and scattering takes place perpendicular to the line grating

primary beam and each other. The sample was placed on a rotating platform with the line direction of the grating aligned in parallel with the rotation axis. Its range of rotation extended from -50° to 50° with a step of 1° , and the data collection time at each angle was 10 s. A reciprocal space map (RSM) was constructed to facilitate the visualization of the diffraction data from all the tilt conditions simultaneously. The reciprocal space map representation was prepared by extracting the diffracted intensities from each individual tilt condition into a one-dimensional scattering profile.

$$|\mathbf{q}| = \frac{4\pi}{\lambda} \sin \theta \tag{1}$$

$$\Delta \mathbf{q} = \frac{2\pi}{L} \tag{2}$$

The scattered intensity $I(q)$ of the system was recorded as a function of the scattering vector q , the modulus of which can be obtained from Eq. (1), where 2θ is the angle of diffraction (see Fig. 2) and λ is the X-ray wavelength. The diffraction peak separation is given by Eq. (2), where L is the period of the grating sample, thus facilitating the straightforward acquisition of pitch information. The critical dimensions describing the nanostructure were determined by the relative intensity and profile of the peaks at different rotation angles ω relative to the incidence.

$$A_f(\mathbf{q}) = \sum_T \int_A \rho(\mathbf{r}) * \sum_n \delta(x - nL) \exp(-i\mathbf{q}\mathbf{r}) \, d\mathbf{r} \tag{3}$$

$$I_f(\mathbf{q}) = |A_f(\mathbf{q})|^2 \tag{4}$$

$$I(\mathbf{q}) = I_f(\mathbf{q}) \exp(-i\mathbf{q}^2 \sigma_{\text{DWF}}^2) \tag{5}$$

The three-dimensional configuration of the lines is depicted through a sequence of form factors that are convoluted with structural factors from an ideal grating. The general form of the scattering intensity in CD-SAXS was calculated using Eqs. (3)–(5), where $\rho(r)$ is the shape function [30, 31], L is the pitch, and $*$ denotes the convolution operation. The Debye–Waller factor σ_{DWF} describes interfacial roughness. In this application, the Fourier transform of each trapezoid in the model is computed, and the results are aggregated to determine the amplitude $A_f(\mathbf{q})$, which is then used in the calculation of $I_f(\mathbf{q})$. The structural factors of the grating reflected the periodic information of the grating nanostructure. Because the Voigt profile serves as a theoretical natural description of the shape of the diffraction peaks, the Voigt function's profile can be adjusted by tuning its parameters to match the shape of each diffraction peak in the CD-SAXS experimental results [32]. Using the structure factor, each Voigt profile is constrained to periodic positions along the q_x direction, defined by the pitch L . In practice, the structure factor can be constructed by convoluting the Voigt profile with a one-dimensional lattice of Dirac delta functions in the q_x direction.

The analysis of CD-SAXS involves an inverse and iterative approach. This method compares the scattering calculated from a hypothesized form function with actual scattering data. The trial shape was adjusted iteratively until the calculated scattering aligned with the observed scattering data. The influence of various parameters on the form factor of the trapezoidal grating sample is shown in Fig. 3. These graphs show that different critical grating dimensions have varying effects on the shape factor. A comparison of the

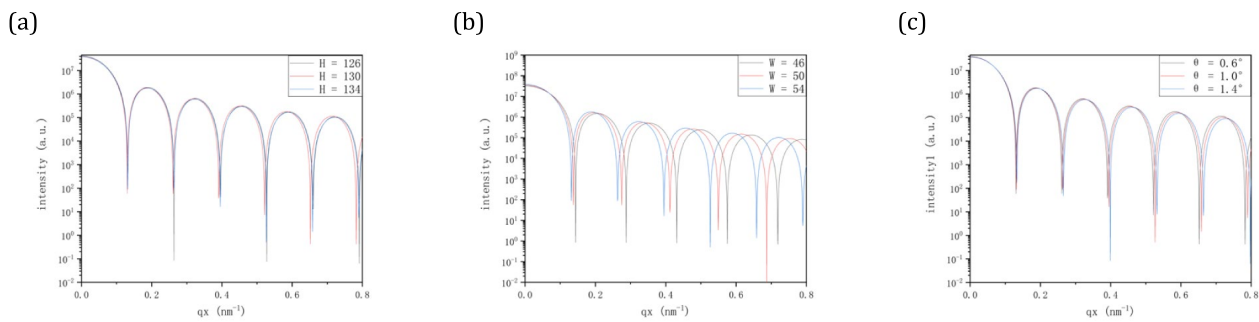


Fig. 3 (Color online) The impact of parameters on shape factor profile **a** height (H), **b** grating width (W), **c** sidewall angle (SWA)

influence of each parameter aids in adjusting their ranges to fit the experimental data more accurately.

2.2 Curve fit

Curve fitting is a prevalent technique in science and engineering for approximating the functional relationships represented by discrete data points [33–36]. Mathematically, these discrete data points can be represented using continuous curves or densely packed discrete equations. This enables mathematical calculations, theoretical analysis of experimental results, and estimation of unmeasurable locations. This method plays a crucial role in solving several problems that rely solely on sampling or experimentation to acquire discrete data.

The fitting of the experimental data is framed as an optimization problem with the fitting function's undetermined parameters, such as the critical dimensions in CD-SAXS. The objective of the optimization was to minimize a certain error metric between the observed experimental data and the function values of the fitting function. A typical optimization goal is to minimize the sum of the squares of the errors between the values of the fitting function and observed data. Alternatively, in cases where the significance or distribution of the observed data varies, a weighted sum of squares of errors can be employed as the optimization objective [37, 38].

$$\min J(p_1, \dots, p_m) = \sum_{i=1}^n [y_i - f(x_i)]^2 \quad (6)$$

The least squares approach is a fundamental method for data fitting. For the observed data (x_i, y_i) , $(i = 1, 2, \dots, n)$, the objective function of the optimization problem is to minimize the sum of the squared errors between the observed experimental data y_i and the calculated values $f(x_i, p)$ of the fitting function $f(x_i)$, as illustrated in Eq. (6). (p_1, \dots, p_m) represent the undetermined parameters within the fitting function.

The theoretical computation of CD-SAXS involves parameters related to several critical dimensions, along with considerations for describing the width of diffraction peaks. Given the high-dimensional parameter space formed by the parameters to be fitted, navigating for optimal solutions within vast datasets poses significant challenges, and an advanced curve fitting approach was employed, combining a stepwise fitting strategy with an iterative optimization process. Initially, traditional gradient descent methods were tested but proved inadequate for locating the global optimum within the complex parameter space. Instead, a stepwise fitting approach was adopted, beginning with data visualization and focusing on analyzing the impact of each parameter on the function's graph. Firstly, partial parameter fitting is performed on specific parameters without considering the influence of others, thereby reducing the dimensionality of the parameter space. Subsequently, an iterative optimization strategy is applied, where multiple starting points are randomly selected within the parameter space, and the loss function (mean squared error) is evaluated for each iteration. The minimum value of the loss function is identified as the optimal solution. To ensure reproducibility, the random seed for the starting points is fixed, and the fitting process is repeated multiple times to confirm consistency. This combined approach has been shown to significantly improve the accuracy and reliability of the fitting results, thereby enabling efficient navigation of the high-dimensional parameter space in CD-SAXS measurements.

2.3 Measurement error analysis

To ensure the reliability of the measurements, all experimental conditions other than the variables of interest (beam size and X-ray energy) were carefully controlled. The sample environment, detector settings, and other instrumental parameters were kept constant throughout the experiments. Data collection began only after the system had stabilized following changes in beam size or X-ray energy. This rigorous control of the experimental conditions minimized potential interference

and ensured the validity of the results. The raw experimental data were preprocessed to ensure accuracy and reliability. Outliers such as those caused by detector defects (e.g., bad pixels) were identified and removed. Given the large number of data points involved in the CD-SAXS fitting, the removal of outliers did not significantly impact the overall dataset. In addition, the data were normalized to facilitate background scattering subtraction, which reduced the influence of background noise on the fitting process. This normalization step is critical for improving the precision of the subsequent analysis.

$$q = \frac{4\pi \sin \theta}{\lambda} \tag{7}$$

$$\Delta q = \frac{4\pi \sin(\theta + \Delta\theta)}{\lambda} - \frac{4\pi \sin \theta}{\lambda} \tag{8}$$

In small-angle X-ray scattering experiments, Eq. (7) provides a fundamental tool for describing the relationship among the scattering angle θ , scattering wavelength λ , and scattering vector \mathbf{q} . Simultaneously, Eq. (8) offers a method for analyzing the uncertainty of the scattering vector. In this equation, $\Delta\theta$ represents the scattering angle error caused by the pixel size, with each pixel size being fixed for the detector used in the CD-SAXS measurements. As the energy of the X-rays increases, their scattering wavelength λ decreases, resulting in a decrease in the corresponding scattering angles for each scattering vector \mathbf{q} . In such cases, the impact of the scattering angle error $\Delta\theta$ induced by the pixel size in $(\theta + \Delta\theta)$ increases. This results in an increased uncertainty in the scattering vector. This suggests that the increased X-ray energy corresponds to an elevated signal error detection. This analysis provides insights into the potential sources of errors when conducting small-angle X-ray scattering experiments at different energies. It is important to take appropriate measures to maximize the accuracy and reliability of experimental data.

The detector enables precise measurement of the scattered signal intensity. Processing the collected data allowed for the determination of the peak center position. Typically, the position of the maximum intensity value in the collected data corresponds to the center of the peak. However, the pixels of the detector have a finite size, which introduces an inherent error in determining the peak center position within a pixel-sized area. The error in the peak center position caused by the pixel size can be described using the uncertainty of the scattered signal, as expressed in Eq. (9) as follows:

$$\frac{\Delta q}{q} \sim \frac{1}{2\theta} \sqrt{\alpha^2 + \left(\frac{d}{L}\right)^2 + \left(\frac{\text{PSF}}{L}\right)^2} + \frac{\Delta\lambda}{\lambda}, \tag{9}$$

where θ is the scattering angle, α is the beam divergence, d is the size of the beam, PSF is the point spread function of the small-angle detector, L is the distance from the sample

to the detector, and $\Delta\lambda/\lambda$ is the energy resolution of the incident X-ray flux.

In the CD-SAXS measurement experiments, the distance between the sample and detector was kept constant. Notably, a decrease in the beam size d , as depicted in Eq. (9), results in a reduction in the $\Delta\mathbf{q}/\mathbf{q}$ value. This implies enhanced accuracy for the measurement results for each scattering vector \mathbf{q} . Therefore, a smaller beam size is associated with more precise measurement results. However, the influence of pixel size on the results must be considered. When the beam size is sufficiently small, the detector cannot provide the necessary resolution to accurately measure the scattering vector \mathbf{q} because of the constraint of the pixel size. If overly small, the beam size can narrow the full width at half maximum (FWHM) of the diffraction peak and thus challenge the detector's ability to accurately characterize the peak's shape and adversely affect the accuracy of the results. Selecting a reasonable beam size for a given application is essential to ensure accurate measurement results and overcome the limitations of detector resolution.

As the scattering angle θ increased, the uncertainty of the scattered signal decreased. Therefore, as the magnitude of the scattering vector \mathbf{q} increases, the signal uncertainty decreases. Utilizing the center position of the peak value of the first-order diffraction peak to determine the periodic information of the grating, the period of the sample was inaccurate because of the influence of uncertainty. This uncertainty is further enhanced by increasing the scattering vector \mathbf{q} . This phenomenon is evidenced by the concordance between the theoretical peak positions of the lower-order diffraction peaks and the corresponding experimental data, whereas there is a difference between the theoretical peak positions and the experimental data peak positions of the higher-order diffraction peaks.

Considering the characteristics of the structure factor in CD-SAXS, the positions of the higher-order diffraction peaks can be used to determine the grating period. In this process, the uncertainty in the scattering signal caused by a single pixel can be divided into multiple portions, to reduce the overall uncertainty and consequently minimizing errors in fitting the grating period.

Meanwhile, gaps between the pixels from some detectors may lead to undetected peak values in the diffraction patterns, rendering the sole reliance on the maximum intensity for determining the diffraction peak centers inaccurate. The shape and positional information of each diffraction peak can be accurately determined through the method of fitting the diffraction peaks. To mitigate this deviation, a multi-peak fitting approach was employed to fit the diffraction peaks in the experimental results, while simultaneously obtaining the position information for each diffraction peak. The final fitting results aligned the peak centers of the structure factor with the diffraction peaks in the experimental

results, thereby enhancing the accuracy and reliability of the measurement results.

In the process of fitting the diffraction peaks, the full width at half maximum (FWHM) determines the shape and subsequently helps ascertain the peak center position. Insufficient data points can lead to imprecise measurements of the FWHM, which can affect both the peak fitting and final autocorrelation coefficient.

Although narrower diffraction peaks facilitate peak position localization, they offer less data, which limits the details of the peak information. This scarcity of data complicates the distinction of the background noise in the overall fitting process. Therefore, selecting an appropriate beam size is crucial to obtain accurate fitting results.

3 Results and discussion

3.1 Effect of different beam sizes

Table 1 presents a comparative analysis of the CD-SAXS results with those of other measurement techniques to evaluate performance. Scanning Electron Microscopy (SEM) can provide information on the grating pitch without delving into the depth of the grating, thus preserving sample integrity. By contrast, Atomic Force Microscopy (AFM) can theoretically measure the grating depth. However, because of the relatively coarse nature of AFM probes at critical scales, crucial information within the surface topographic images may be obscured, leading to potential inaccuracies. Moreover, limitations may arise during grating depth measurements, restricting the probe's access to the bottom of the grooves owing to neighboring gratings. Consequently, AFM struggles to provide precise depth-oriented details, offering only periodic information within the scanned grating sample.

The Optical Critical Dimension (OCD) yields depth information but requires referencing results from AFM and SEM before the data fitting process. Accurate period determination in OCD measurements is critical for obtaining precise structural size information. Figure 4 shows the measurement results of the gratings obtained using SEM, AFM, and OCD.

This study investigated the effects of various beam sizes on data acquisition and precision during the experimental

process. Four distinct beam sizes were identified on the grating sample at the small-angle X-ray scattering beamline, with the smallest spot designated as P1 and the largest as P4. The beam sizes were arranged in ascending order. Figure 5 shows the shapes and dimensions of beams P1–P4,

It is acknowledged that there is a degree of human error inherent in the process of sample placement. Consequently, the results for each measured angle were affected by an error in the initial angle. In order to compensate for the error in the initial angle, the symmetry shown in Fig. 6 can be utilized. Reconstructed images of CD-SAXS measurements from different angles and different beam sizes produce an intensity map as a function of q_x and q_z , as shown in Fig. 6.

For the CD-SAXS measurements, a silver behenate sample was used to calibrate the distance from the sample to the detector, which was set to approximately 2.95 m. When a fixed sample-to-detector distance is maintained, a smaller beam may result in data loss near the full width at half-maximum (FWHM) of the diffraction peak, as shown in Fig. 7. Detailed analysis of the results obtained from the P1 group showed that each peak existed independently in a one-dimensional curve. The measured data points were mainly distributed around the peak values of the diffraction peaks and between the neighboring diffraction peaks.

Although this experiment rapidly determined the diffraction peak positions, the significant drawback is the shortage of data points near the half-maximum of the diffraction peaks, which is a phenomenon evident in the P1 curve illustrated in Fig. 7. In the process of fitting the diffraction peaks, FWHM was employed to determine the peak shapes and subsequently to determine the positions of the peak centers. The scarcity of data points resulted in large absolute values of the derivatives at the diffraction peaks' half-maximum positions, making it difficult to accurately determine the FWHM of the peak shapes. Insufficient data points led to inaccurate measurements of the width at half-maximum, which in turn affected the fitting of the diffraction peaks and, thus the final autocorrelation coefficient.

Figure 8 reveals considerable dispersion in the P1 data points, particularly in the q_z direction, where the number of data points is comparatively lower than in the other groups. This scarcity of data points makes it challenging to discern the true trend, leading to a decrease in the fitting accuracy and rendering the fitted values less reliable. Notably, the data at $q_x = 0.252 \text{ nm}^{-1}$ were particularly susceptible to noise, which hinders a comprehensive assessment of the overall trend of the experimental data. This increased difficulty in separating the background signals complicates the distinction between useful signals and background noise. Consequently, the fitting algorithm may overfit the noise, leading to significant deviations of the fitted values from the expected experimental outcomes.

Table 1 Comparison of the SEM, AFM, OCD, and CD-SAXS measurements

	SEM	AFM	OCD	CD-SAXS
Pitch (nm)	98.3	102.3	–	100.5 ± 0.2
Width (nm)	49.1	–	49.6	50.0 ± 0.6
Height (nm)	–	–	129.1	131.3 ± 0.4
Sidewall angle (°)	–	–	1.3	1.1 ± 0.1

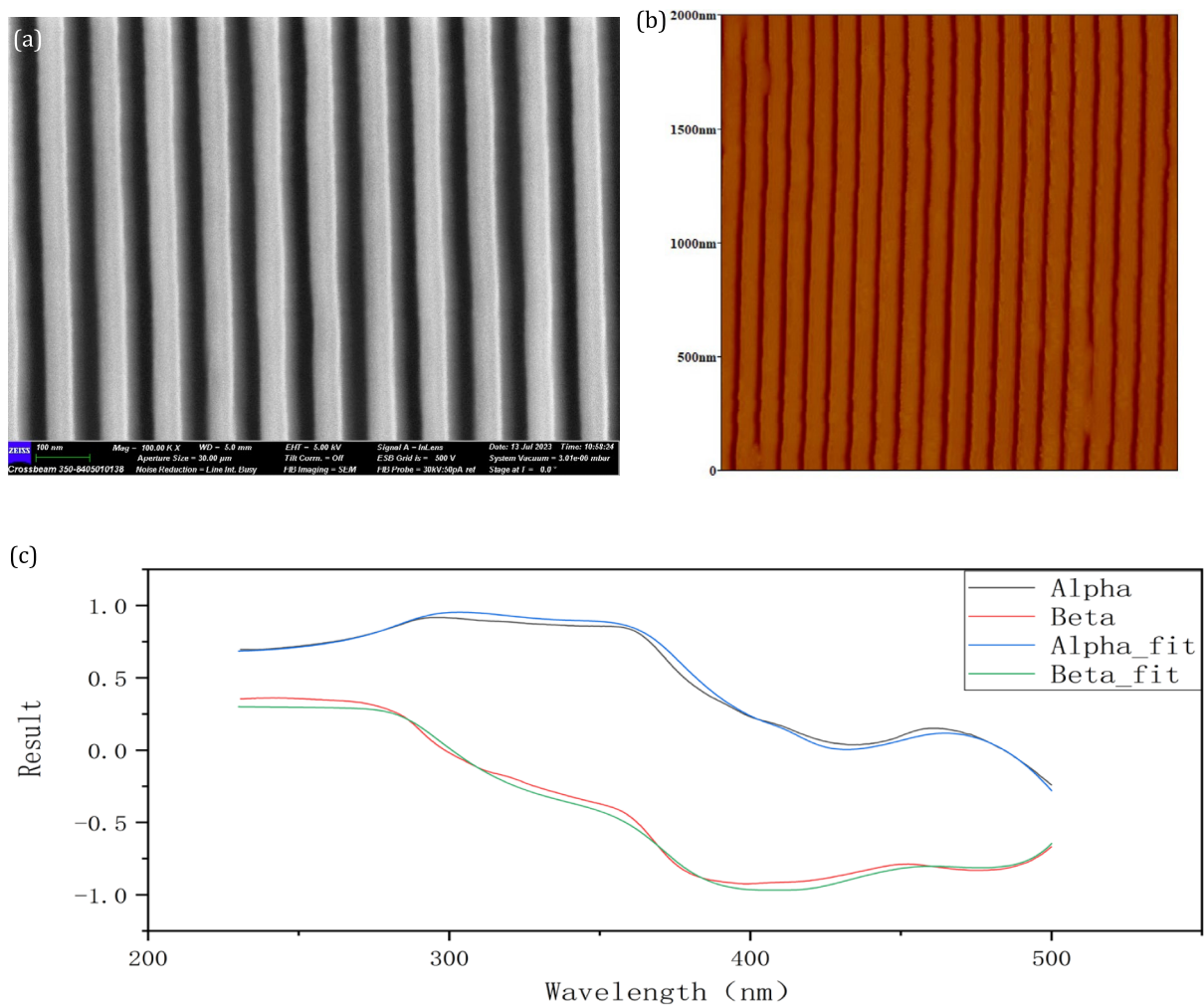


Fig. 4 (Color online) **a** is the result of SEM measurement of grating, **b** is the result of AFM measurement of grating, **c** is the spectral fitting result of OCD measurement of grating

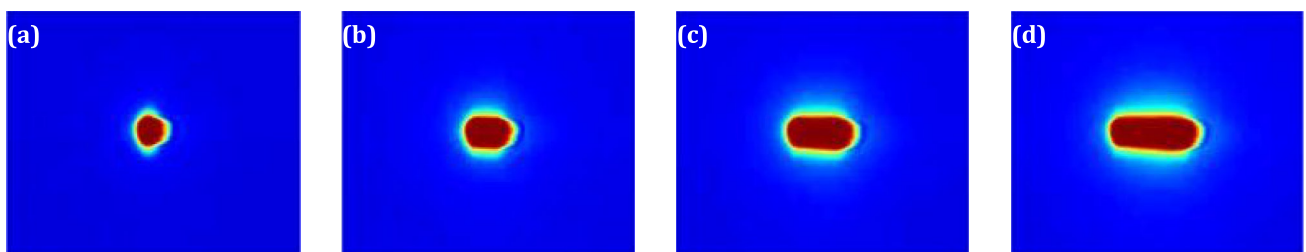


Fig. 5 (Color online) The four different beam sizes used in CD-SAXS measurement experiments. **a** Picture (a) shows the initial beam size, and the experiment performed on this beam is named P1. The beam

sizes corresponding to **(b–d)** are, respectively, 2, 3, and 4 times the original beam size. The experiments corresponding to these groups are designated as P2–P4

The results of CD-SAXS measurements using different beam sizes are summarized in Table 2. Observing the results, measurements with the smallest beam size exhibited the smallest pitch confidence interval. Although the results

in this group showed minor differences in grating width, height, and sidewall angle compared to the expected values (i.e., the known critical dimensions of the reference material (RM) used in our experiments), the confidence interval for

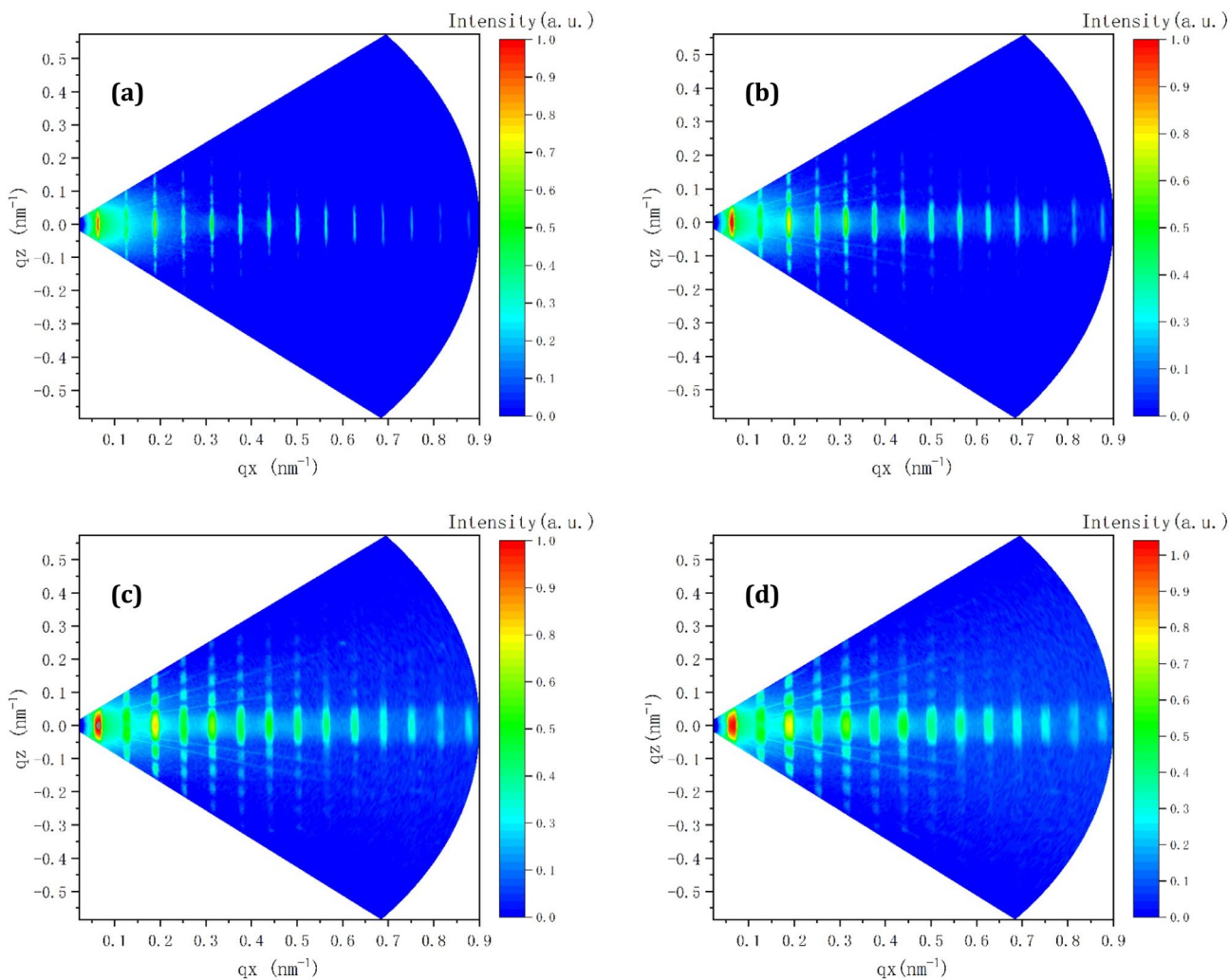


Fig. 6 (Color online) **a** is the q_x - q_z intensity map obtained by the CD-SAXS measurement of the P1 group, **b-d** are the results of the P2-P4 group

the sidewall angle was notably large. Even if many experiments were completed, the sidewall angle remained at a higher level of uncertainty in the P1 group. The significant sidewall angle uncertainty for P1 was derived from the small beam size, which resulted in experimental data that did not accurately describe the shape of the diffraction peaks. Therefore, it is challenging to provide precise information regarding shape factors. A moderate increase in the beam size for group P2 notably narrowed the confidence interval without evident deviations in the fitting results. Conversely, further beam size increases in P3 and P4 increase the uncertainty of the critical dimensions. Specifically, the fitting results for group P4 deviated noticeably from those of the other groups and the expected values, substantially reducing the measurement precision. The deviation observed in the results can be attributed to the relatively large beam size, resulting in a set of diffraction peaks with comparatively smooth and broadened profiles owing to the smear effect of scattering. This

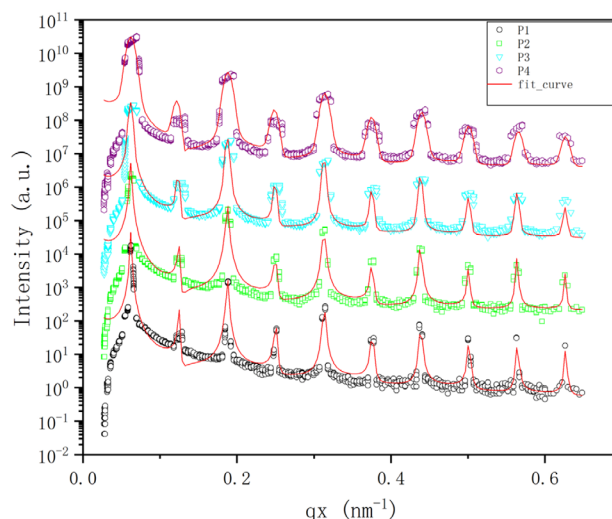


Fig. 7 (Color online) In the experiments with the four different beam sizes, fit experimental data as a function of q_x at $q_z = 0$ using the least squares method, the circles are raw data and the lines represent the fitting

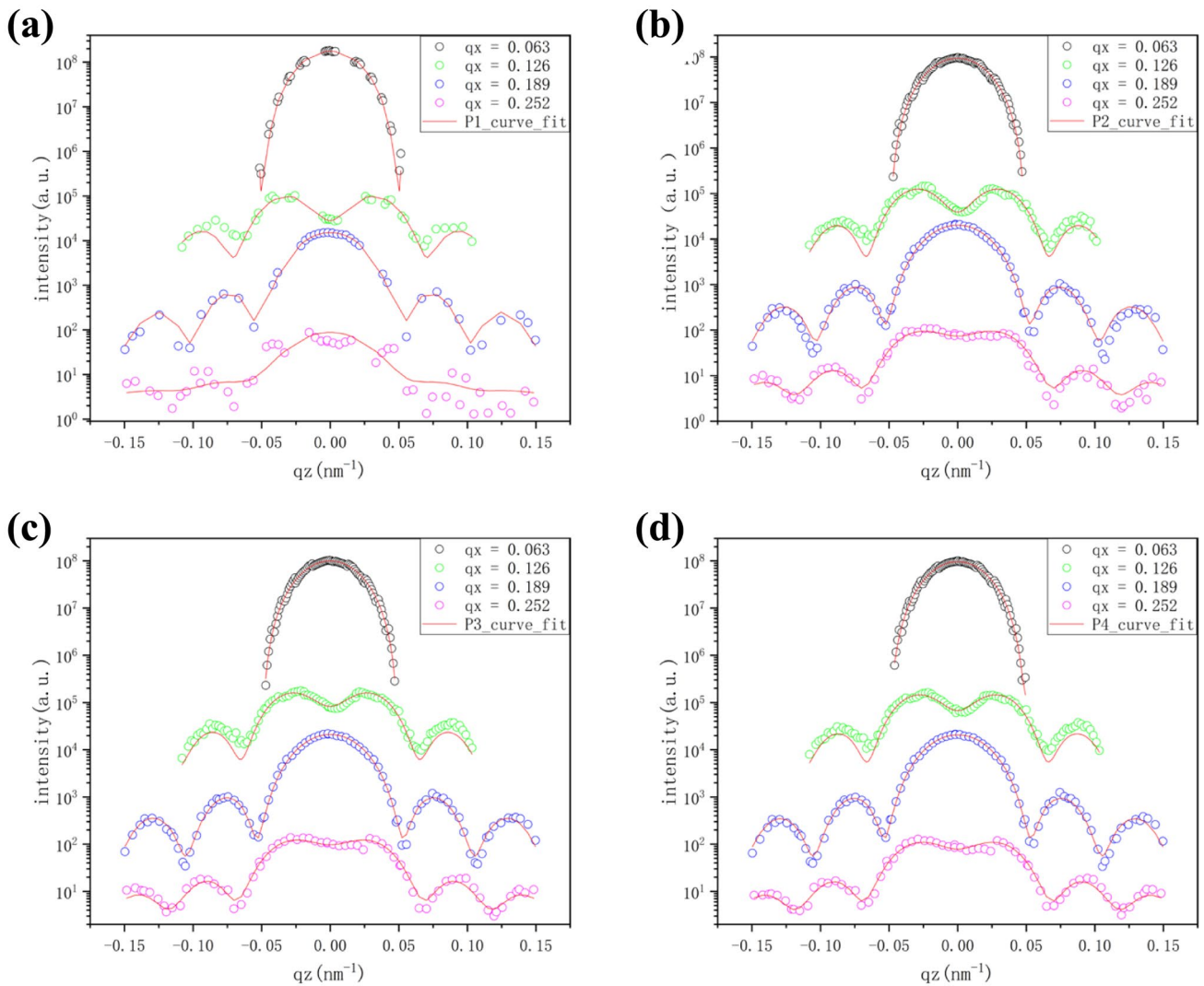


Fig. 8 (Color online) In the experiments with the four different beam sizes, **a–d** correspond to the results obtained from the experiments of groups P1–P4. The scattering intensity along vertical q_z slices at

evenly spaced intervals in q_x , obtained from reciprocal space maps, the circles are raw data and the lines represent the fitting

broadening of the peak profiles led to increased uncertainty in confirming the exact locations of the peak centers. In the context of CD-SAXS data fitting, it is imperative to use the values of the diffraction peaks to discern the shape factor trend, thereby extracting crucial dimensional information regarding the grating sample. The increased uncertainty in

peak center identification renders the fitting algorithm more vulnerable to nearby values, thus diminishing the emphasis on peak centers and adversely affecting the shape factor determination and fitting precision. These findings highlight the significant impact of beam size on the uncertainty and precision of CD-SAXS measurements. Therefore, an appropriate beam size selection is crucial for obtaining accurate and reliable measurement results, ensuring the credibility and reproducibility of the experimental results.

Table 2 Comparison of results from four spot sizes

Parameter	P1	P2	P3	P4
Pitch (nm)	100.3 ± 0.1	100.4 ± 0.2	100.5 ± 0.2	100.5 ± 0.3
Width (nm)	49.8 ± 0.6	49.8 ± 0.2	50.0 ± 0.6	50.3 ± 0.6
Height (nm)	130.3 ± 0.4	130.0 ± 0.2	130.3 ± 0.3	131.4 ± 0.5
Sidewall angle (°)	1.1 ± 0.5	1.1 ± 0.2	1.2 ± 0.2	1.2 ± 0.3

3.2 Effect of different energies

To thoroughly analyze the impact of X-ray photon energy on CD-SAXS measurement accuracy, this study performed CD-SAXS assessments of gratings using various X-ray photon

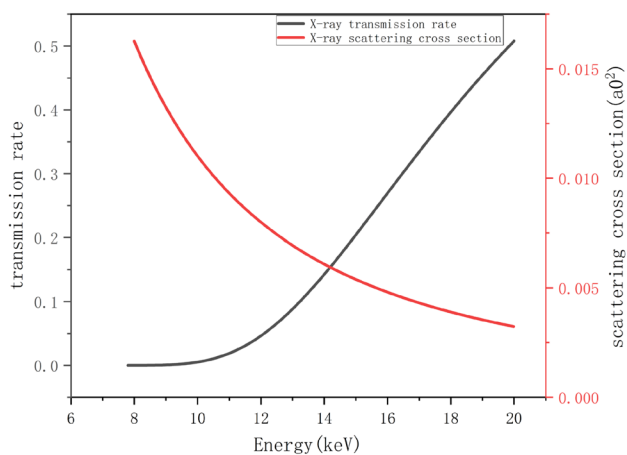


Fig. 9 (Color online) X-ray transmission rate and scattering cross section at different energies. The unit of scattering cross section is a_0^2 , where $a_0^2 = 2.8002852 \times 10^{-21} \text{ m}^2$

energies while maintaining a constant beam size. In CD-SAXS experiments, scientists at NIST recommend conducting tests at energy levels greater than 17 keV. High-energy X-rays facilitate straightforward transmission through the grating sample substrate. However, this simplicity comes at the cost of reduced interaction between the X-rays and grating. Figure 9 shows the transmission rate of X-rays through a $700 \mu\text{m}$ silicon substrate at different energy levels. When the X-ray photon energy was high, the absorption of the grating sample decreased and the transmittance increased. This results in background scattering that passes through the grating and is received by the detector. To perform CD-SAXS measurements using laboratory X-ray sources, the challenge of low intensities must be addressed when performing CD-SAXS measurements using laboratory X-ray

sources. Achieving high-quality scattering signals within a short time frame necessitates an improvement in photon utilization efficiency. Therefore, careful selection of the metal target in the X-ray tube is crucial for designing laboratory X-ray sources. By contrast, synchrotron radiation sources produce X-rays with exceptionally high brightness, resulting in a significantly elevated photon flux per unit area. This characteristic allows researchers to acquire a substantial amount of information from a detector within a given time period. The use of synchrotron radiation sources for CD-SAXS experiments at various X-ray photon energy levels can serve as a reference for selecting metal targets when constructing laboratory X-ray sources.

The reconstructed images from CD-SAXS measurements produced an intensity map as a function of q_x and q_z , as shown in Fig. 10a. The 16 keV test results revealed numerous diffraction peaks, and the peak centers of these diffraction peaks can provide information about the structural factor of the trapezoidal grating sample.

As shown in Fig. 10b, a detailed examination of the data is achieved through one-dimensional profile cuts over q_x ($q_z = 0$) and q_z (across all peak orders). The lack of clear spacing between diffraction peaks significantly increases the mutual interference, and excessively broad peaks reduce the resolution, which complicated the identification of the peak positions. A high resolution is crucial for CD-SAXS measurements to accurately determine periodic information. Observations at 16 keV revealed a notable broadening of the diffraction peaks, which caused adjacent peaks to obscure each other, with significant intensity variations. The second-order diffraction peak is heavily influenced by the first-order peak, posing challenges for accurate observation. Furthermore, peak widening considerably decreases the signal-to-noise ratio, creating uncertainty in the relative

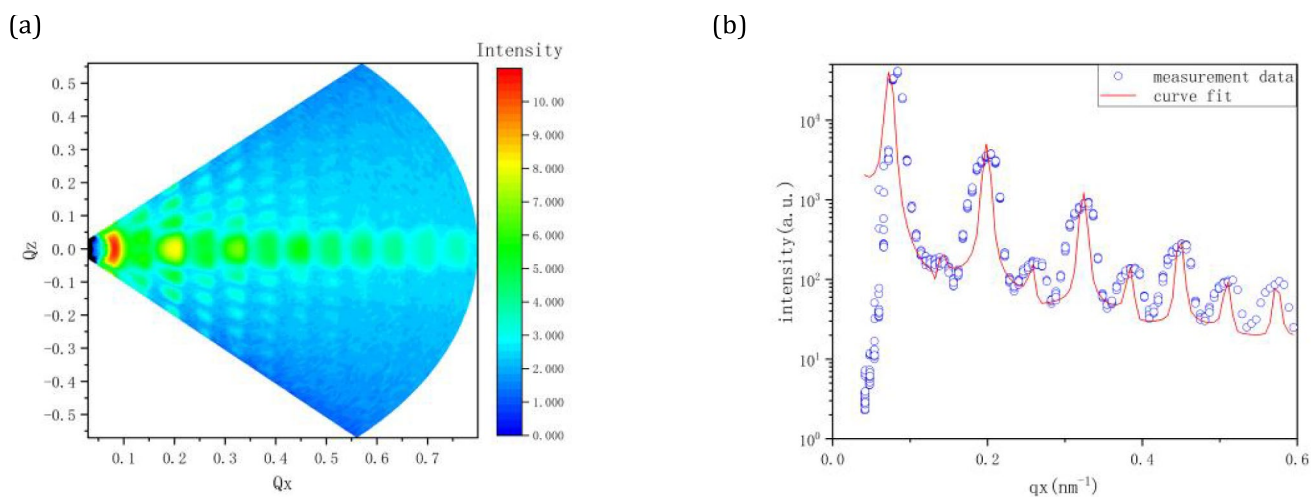
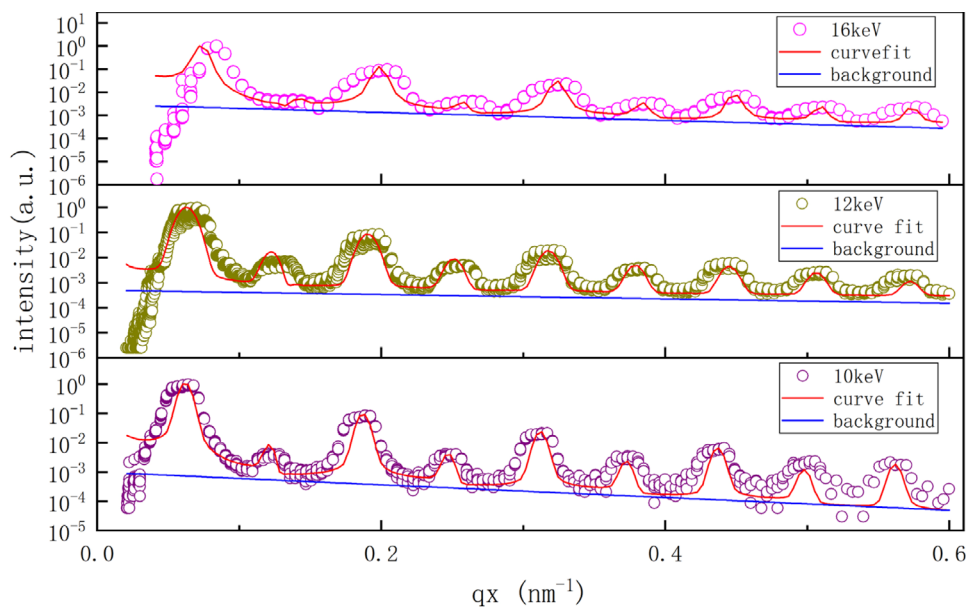


Fig. 10 (Color online) **a** $q_x - q_z$ intensity map obtained from CDSAXS measurements at 16 keV. **b** In the $q_z = 0$ cut, it is clearly visible that there is overlap between the diffraction peaks

Fig. 11 (Color online) In the experiments with the three different energies, fit experimental data as a function of q_x at $q_z = 0$



intensity correlation between the signals and noise. Consequently, this decreases the accuracy of the fitting results and markedly increases the uncertainty.

The CD-SAXS results obtained at 10 keV and 12 keV are shown in Fig. 11. These results were normalized to facilitate the analysis of the energy effect with various scattering cross sections on the experimental results. Although the X-ray transmissivities at 10 keV and 12 keV were lower than those at 16 keV, the diffraction peaks were clearly distinct and did not overlap. The clear shapes of the diffraction peaks are advantageous for data fitting. In addition, the diffraction peaks were distinctly separated from the background scattering. There were significant differences in the peak heights and background intensities, which made them easy to distinguish. Higher X-ray photon energy leads to increased background scattering, as shown in Fig. 11. This decreased contrast can impair the accuracy of the peak measurement and analysis. As the X-ray energy increased, the absorption capacity of the grating sample decreased, whereas the penetration capacity increased. This implies that a larger number of X-ray photons can pass through the substrate, accompanied by a corresponding enhancement in the background signals that pass through the sample and are received by the detector. Concurrently, the scattering cross section decreases, resulting in weakening of the intensity of each scattering event. An overall enhancement of the diffraction peak and background signals was observed; however, the signal-to-noise ratio decreased. Figure 9 shows the calculation of the scattering probability at each energy level, demonstrating that as the energy increases, the scattering probability also increases. The enhancement of the background signal reduces the signal-to-noise ratio of the diffraction pattern, which in turn results in the boundaries of

the diffraction peaks becoming blurred and increasing their width. The analysis of the grating structure becomes more complex because of the indistinct positions and different diffraction peaks.

In the experimental results at 10 keV and 12 keV, we can readily observe that the background scattering remains stable between the diffraction peaks and is unaffected by the presence of diffraction peaks. This reduces the uncertainties introduced by noise during the fitting process. The CD values obtained at three different energies are listed in Table 3.

This confirmed the feasibility of CD-SAXS testing below 17 keV. As the energy of the X-rays increased, the grating parameters achieved an optimal solution, which occurred when the energy of the X-rays was 12 keV. The mean values of the height, sidewall angle, and pitch at 16 keV exhibited a notable discrepancy from the expected values. The mean width at 10 keV exhibits a considerable discrepancy from the expected value. Notably, the measurement results at 12 keV exhibit the smallest confidence interval. Compared with the other two sets of results, the data at 12 keV were more accurate and relatively stable.

The dependences of CD on the X-ray beam size and photon energy are shown in Fig. 12. Clearly, the changes in these conditions affect the average measurement values and allow easy observation of the confidence intervals for each dataset. By comparing the size of the grating standard sample, different experimental conditions with high precision and small confidence intervals. This provides a basis for determining the experimental conditions for future CD-SAXS measurements.

Table 3 Comparison of CD-SAXS measurements with different energies

Parameter	10 keV	12 keV	16 keV
Pitch (nm)	100.8 ± 0.5	100.6 ± 0.3	101.1 ± 1.2
Width (nm)	51.0 ± 0.9	50.1 ± 0.4	50.4 ± 2.4
Height (nm)	131.9 ± 1.7	131.2 ± 1.3	132.4 ± 3.1
Sidewall angle (°)	1.3 ± 0.7	1.2 ± 0.3	1.4 ± 0.4

4 Conclusion

In this study, the critical dimensions of a grating with a half-pitch of 50 nm were investigated using small-angle X-ray

scattering with various spot sizes and incidence energies. We propose an effective fitting method for reconstructing grating structural information and obtaining the critical dimensions. The optimized CD values were achieved with an X-ray energy of 12 keV and a spot size of 200 μm , with a precisions of 0.2 nm for the pitch, width, and height, as well as 0.1° for the sidewall angle (SWA). This research demonstrates the significance of the beam size and confirms the viability of CD-SAXS experiments within specific energy ranges, laying the foundation for future developments and providing valuable references for laboratory setups. In conclusion, this study makes a significant contribution to CD-SAXS experimentation and paves the way for further technological advancements.

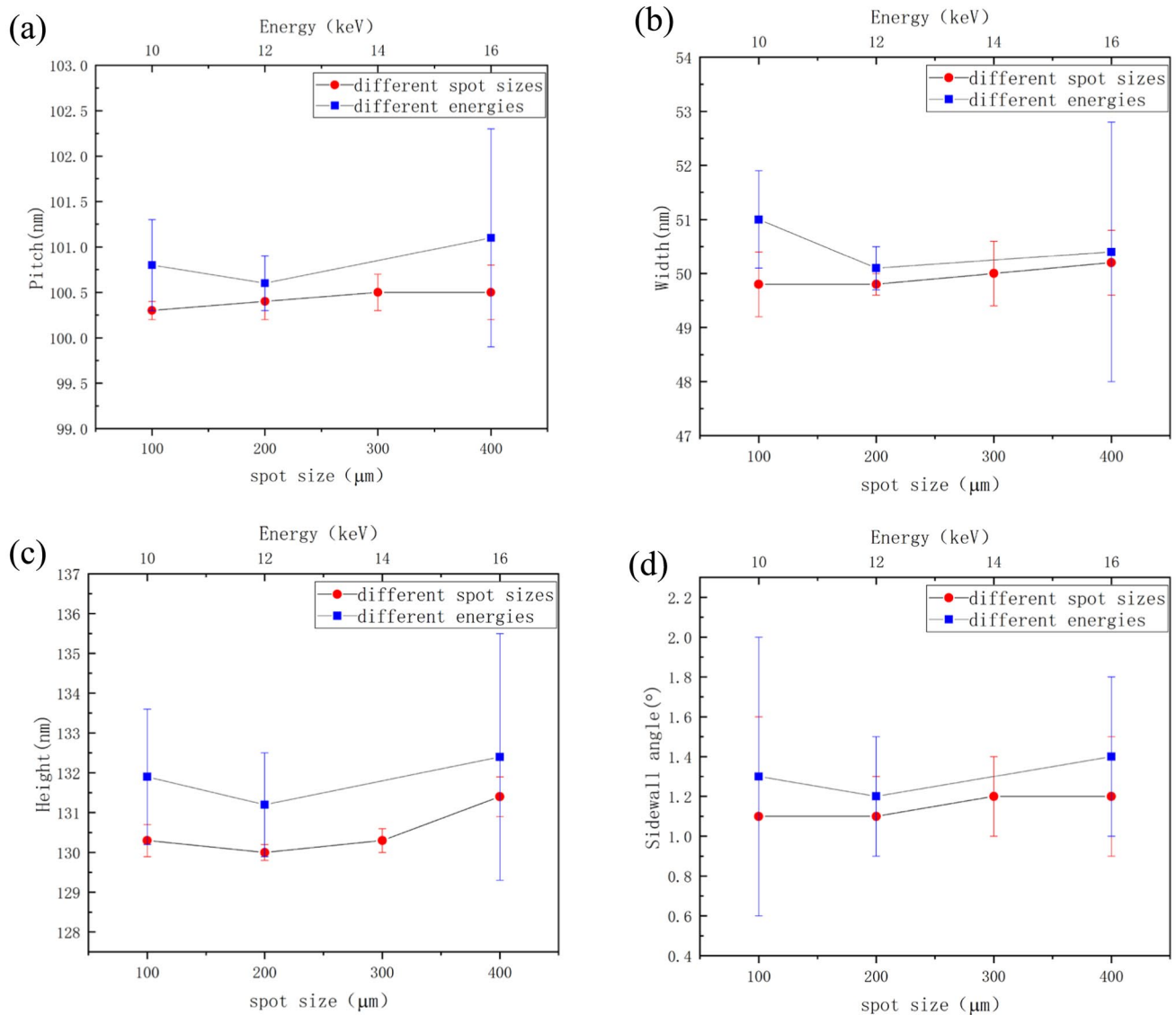


Fig. 12 (Color online) Measurement of critical dimensions of gratings using SAXS with varying energies and spot sizes. **a** Shows the pitch information of gratings measured in each group of CD-

SAXS measurements (**b–d**), respectively, show the width, height and side wall angle information of the grating

Despite its advantages, CD-SAXS technology faces several challenges that limit its current applicability. One major limitation is the requirement for a high signal-to-noise ratio (SNR) to accurately infer the key dimensions from the data. Achieving a high SNR often requires prolonged irradiation times, which can be impractical for routine laboratory use. Additionally, the low flux of laboratory X-ray sources further restricts the efficiency of CD-SAXS measurements. To address these challenges, the Mo X-ray source emerges as a favorable choice due to its balanced performance characteristics. However, the liquid-metal-jet X-ray source—particularly alloy-rich indium variants—presents a promising alternative, because it enhances the flux density by one order of magnitude while achieving smaller spot sizes (100 μm) compared with solid-target sources (500 μm with multilayer-coated Montel mirrors). These advancements align directly with our CD-SAXS measurement accuracy results, where the reduced spot size and enhanced flux synergistically improve the precision. Future efforts should prioritize optimizing such high-brightness sources along with algorithmic innovations to streamline data acquisition and analysis, and ultimately accelerate the adoption of CD-SAXS in both research and industrial metrology.

Acknowledgements This work was also supported by the User Experiment Assist System of Shanghai Synchrotron Radiation Facility (SSRF). The authors thank the beamline scientists at beamlines (BL16B1, BL19U2, BL10U1, and BL08U) of Shanghai Synchrotron Radiation Facility for support and discussions.

Author Contributions C-M Yang contributed to the study conception and design. Material preparation, data collection, and analysis were performed by X-Y Qin, C-M Yang, and F-G Bian. The first draft of the manuscript was written by X-Y Qin, and all authors commented on previous versions of the manuscript. All authors read and approved the final manuscript.

Data availability The data that support the findings of this study are openly available in Science Data Bank at <https://cstr.cn/31253.11.sciencedb.j00186.00839> and <https://www.doi.org/10.57760/sciencedb.j00186.00839>.

Declarations

Conflict of interest The authors declare that they have no Conflict of interest.

References

- I.L. Markov, Limits on fundamental limits to computation. *Nature* **512**, 147–154 (2014). <https://doi.org/10.1038/nature13570>
- C.A. Mack, Fifty years of Moore's Law. *IEEE Trans. Semicond. Manufact.* **24**, 202–207 (2011). <https://doi.org/10.1109/tsm.2010.2096437>
- H.N. Khan, D.A. Hounshell, E.R.H. Fuchs, Science and research policy at the end of Moore's law. *Nat. Electron.* **1**, 14–21 (2018). <https://doi.org/10.1038/s41928-017-0005-9>
- M.V. Kovalchuk, A.E. Blagov, Y.A. Dyakova et al., Investigation of the initial crystallization stage in lysozyme solutions by small-angle X-ray scattering. *Cryst. Growth Des.* **16**, 1792–1797 (2016). <https://doi.org/10.1021/acs.cgd.5b01662>
- D.F. Sunday, M.R. Hammond, C.Q. Wang et al., Determination of the internal morphology of nanostructures patterned by directed self-assembly. *ACS Nano* **8**, 8426–8437 (2014). <https://doi.org/10.1021/nn5029289>
- D.F. Sunday, J.X. Ren, C.D. Liman et al., Characterizing patterned block copolymer thin films with soft X-rays. *ACS Appl. Mater. Interfaces* **9**, 31325–31334 (2017). <https://doi.org/10.1021/acsami.7b02791>
- C.Q. Wang, R.L. Jones, E.K. Lin et al., Small angle X-ray scattering measurements of lithographic patterns with sidewall roughness from vertical standing waves. *Appl. Phys. Lett.* **90**, 193110 (2007). <https://doi.org/10.1063/1.2737399>
- S. Liu, J. Yang, L. Xu et al., Can ultra-thin Si FinFETs work well in the sub-10 nm gate-length region? *Nanoscale* **13**, 5536–5544 (2021). <https://doi.org/10.1039/D0NR09094H>
- H. Wei, M. Shulaker, H.S. Philip Wong et al., *Monolithic three-dimensional integration of carbon nanotube FET complementary logic circuits*, in *2013 IEEE International Electron Devices Meeting, Washington, DC* (2013), pp. 19.7.1–19.7.4. <https://doi.org/10.1109/IEDM.2013.6724663>
- O. Custance, R. Perez, S. Morita, Atomic force microscopy as a tool for atom manipulation. *Nat. Nanotechnol.* **4**, 803–810 (2009). <https://doi.org/10.1038/nnano.2009.347>
- Y. Yan, X. Tao, G. Xu et al., Modeling the effect of line profile variation on optical critical dimension metrology. *Proc. SPIE* **6518**, 65180Z (2007). <https://doi.org/10.1117/12.704246>
- N.G. Orji, M. Badaroglu, B.M. Barnes et al., Metrology for the next generation of semiconductor devices. *Nat. Electron.* **1**, 532–547 (2018). <https://doi.org/10.1038/s41928-018-0150-9>
- L. Jiang, X.X. Ye, D.J. Wang et al., Synchrotron radiation-based materials characterization techniques shed light on molten salt reactor alloys. *Nucl. Sci. Tech.* **31**, 6 (2020). <https://doi.org/10.1007/s41365-019-0719-7>
- H. Wang, Y.C. Lai, J.J. Zhong et al., Correction of distorted X-ray absorption spectra collected with capillary sample cell. *Nucl. Sci. Tech.* **34**, 106 (2023). <https://doi.org/10.1007/s41365-023-01253-9>
- W.Z. Zhang, J.C. Tang, S.S. Wang et al., The protein complex crystallography beamline (BL19U1) at the Shanghai Synchrotron Radiation Facility. *Nucl. Sci. Tech.* **30**, 170 (2019). <https://doi.org/10.1007/s41365-019-0683-2>
- L. Yang, S. Antonelli, S. Chodankar et al., Solution scattering at the Life Science X-ray Scattering (LiX) beamline. *J. Synchrotron Radiat.* **27**, 804–812 (2020). <https://doi.org/10.1107/S1600577520002362>
- L. Yang, J. Liu, S. Chodankar et al., Scanning structural mapping at the Life Science X-ray Scattering Beamline. *J. Synchrotron Radiat.* **29**, 540–548 (2022). <https://doi.org/10.1107/S1600577521013266>
- R.X. Chen, Y. Song, Z.C. Wang et al., Development in small-angle X-ray scattering (SAXS) for characterizing the structure of surfactant-macromolecule interaction and their complex. *Int. J. Biol. Macromol.* **251**, 126288 (2023). <https://doi.org/10.1016/j.ijbiomac.2023.126288>
- G. Wang, L.F. Xu, J.L. Shen et al., Iterative and accurate determination of small angle X-ray scattering background. *Nucl. Sci. Tech.* **27**, 105 (2016). <https://doi.org/10.1007/s41365-016-0108-4>

20. Y.W. Li, G.F. Liu, H.J. Wu et al., BL19U2: Small-angle X-ray scattering beamline for biological macromolecules in solution at SSRF. *Nucl. Sci. Tech.* **31**, 117 (2020). <https://doi.org/10.1007/s41365-020-00825-3>
21. C.H. Yang, M.J. van der Woerd, U.M. Muthurajan et al., Biophysical analysis and small-angle X-ray scattering-derived structures of MeCP2-nucleosome complexes. *Nucl. Acids Res.* **39**, 4122–4135 (2011). <https://doi.org/10.1093/nar/gkr005>
22. D. Huang, C.X. Hong, J.H. Han et al., In situ studies on the positive and negative effects of 1,8-diiodooctane on the device performance and morphology evolution of organic solar cells. *Nucl. Sci. Tech.* **32**, 57 (2021). <https://doi.org/10.1007/s41365-021-00893-z>
23. X.Z. Dai, C.B. Fei, P. Kandlakunta et al., Origin of the X-Ray-induced damage in perovskite solar cells. *IEEE Trans. Nucl. Sci.* **69**, 1850–1856 (2022). <https://doi.org/10.1109/TNS.2022.3190200>
24. R.L. Jones, T.J. Hu, E.K. Lin et al., Small angle X-ray scattering for sub-100 nm pattern characterization. *Appl. Phys. Lett.* **83**, 4059–4061 (2003). <https://doi.org/10.1063/1.1622793>
25. B.R. Pauw, Everything SAXS: small-angle scattering pattern collection and correction. *J. Phys.: Condens. Matter* **26**, 233201 (2014). <https://doi.org/10.1088/0953-8984/26/23/239501>
26. C. Li, L.L. Han, H. Jiang et al., Three-dimensional crossbar arrays of self-rectifying Si/SiO₂/Si memristors. *Nat. Commun.* **8**, 15666 (2017). <https://doi.org/10.1038/ncomms15666>
27. R. Kline, D. Sunday, C. Wang et al., *Critical dimension small angle X-ray scattering measurements of FinFET and 3D memory structures*, in *27th Conference on Metrology, Inspection, and Process Control for Microlithography, 27th Conference on Metrology, Inspection, and Process Control for Microlithography San Jose* (2013). (Spie-Int Soc Optical Engineering, BELLINGHAM, 2013)
28. C. Wang, R.L. Jones, E.K. Lin et al., Characterization of correlated line edge roughness of nanoscale line gratings using small angle x-ray scattering. *J. Appl. Phys.* **102**, 024901 (2007). <https://doi.org/10.1063/1.2753588>
29. X. Huang, W.C. Lee, C. Kuo et al., Sub-50 nm p-channel FinFET. *IEEE Trans. Electron Device* **48**, 880–886 (2001). <https://doi.org/10.1109/16.91823>
30. B.A. Lippmann, J. Schwinger, Variational principles for scattering processes. *Phys. Rev.* **79**, 469–480 (1950). <https://doi.org/10.1103/PhysRev.79.469>
31. D.F. Sunday, S. List, J.S. Chawla et al., Determining the shape and periodicity of nanostructures using small-angle X-ray scattering. *J. Appl. Crystallogr.* **48**, 1355–1363 (2015). <https://doi.org/10.1107/s1600576715013369>
32. T. Ida, M. Ando, H. Toraya, Extended pseudo-Voigt function for approximating the Voigt profile. *J. Appl. Crystallogr.* **33**, 1311–1316 (2000). <https://doi.org/10.1107/s0021889800010219>
33. A. Ohagan, Curve fitting and optimal design for prediction. *J. R. Stat. Soc. B* **40**, 1–42 (1978). <https://doi.org/10.1111/j.2517-6161.1978.tb01643.x>
34. Y.H. Sun, J.X. Wei, D.S. Xia, Parameter optimization for B-spline curve fitting based on adaptive genetic algorithm. *J. Comput. Appl.* **30**, 1878–1882 (2010). <https://doi.org/10.3724/SP.J.1087.2010.0187>
35. J. Wang, Z.X. Wu, Y.Y. Huang et al., A rapid and accurate gamma compensation method based on double response curve fitting for high-quality fringe pattern generation. *Opt. Laser Technol.* **160**, 109084 (2022). <https://doi.org/10.1016/j.optlastec.2022.109084>
36. Z.S. Shi, Z.H. Wu, Maneuver target detection method with iterative endpoint fitting assisted. *Lecture Notes Electr. Eng.* **256**, 839–846 (2013). https://doi.org/10.1007/978-3-642-38466-0_93
37. A. Fradi, Y. Feunteun, C. Samir et al., Bayesian regression and classification using Gaussian process priors indexed by probability density functions. *Inf. Sci.* **548**, 56–68 (2021). <https://doi.org/10.1016/j.ins.2020.09.027>
38. Q. Li, C. Cheng, S. Guo, Bayesian network classification for aster data based on wavelet transformation. *Proc. SPIE Int. Soc. Opt. Eng.* **5985**, 598532 (2006). <https://doi.org/10.1117/12.657929>

Springer Nature or its licensor (e.g. a society or other partner) holds exclusive rights to this article under a publishing agreement with the author(s) or other rightsholder(s); author self-archiving of the accepted manuscript version of this article is solely governed by the terms of such publishing agreement and applicable law.